

Research article

Instability analysis for MHD boundary layer flow of nanofluid over a rotating disk with anisotropic and isotropic roughness[☆]

Tousif Iqra^a, Sohail Nadeem^{a,b,c}, Hassan Ali Ghazwani^{d,*}, Faisal Z. Duraihem^e, Jehad Alzabut^{b,f}

^a Department of Mathematics, Quaid-I-Azam University 45320, Islamabad 44000, Pakistan

^b Department of Mathematics and Sciences, Prince Sultan University, 11586, Riyadh, Saudi Arabia

^c Department of Mathematics, Wenzhou University, Wenzhou, 325035, China

^d Department of Mechanical Engineering, Faculty of Engineering, Jazan University, P.O. Box 45124, Jazan, Kingdom of Saudi Arabia

^e Department of Mathematics, College of Science, King Saud University, P.O. Box 2455, Riyadh 11451, Saudi Arabia

^f Department of Industrial Engineering, OSTIM Technical University, Ankara 06374, Turkey

ARTICLE INFO

Keywords:

Rough rotating disk
MHD
Nanofluid
Boundary layer flow
Linear stability analysis
Energy production
Energy analysis

ABSTRACT

The study focuses on the instability of local linear convective flow in an incompressible boundary layer caused by a rough rotating disk in a steady MHD flow of viscous nanofluid. Miklavčič and Wang's (Miklavčič and Wang, 2004) [9] MW roughness model are utilized in the presence of MHD of Cu-water nanofluid with enforcement of axial flows. This study will investigate the instability characteristics with the MHD boundary layer flow of nanofluid over a rotating disk and incorporate the effects of axial flow with anisotropic and isotropic surface roughness. The resulting ordinary differential equations (ODEs) are obtained by using von Kármán (Kármán, 1921) [3] similarity transformation on partial differential equations (PDEs). Subsequently, numerical solutions are obtained using the shooting method, specifically the Runge-Kutta technique. Steady-flow profiles for MHD and volume fractions of nanoparticles are analyzed by the partial-slip conditions with surface roughness. Convective instability for stationary modes and neutral stability curves are also obtained and investigated by the formulation of linear stability equations with the MHD of nanofluid. Linear convective growth rates are utilized to analyze the stability of magnetic fields and nanoparticles and to confirm the outcomes of this analysis. Stationary disturbances are also considered in the energy analysis. The investigation indicates the correlation between instability modes Type I and Type II, in the presence of MHD, nanoparticles, and the growth rates of the critical Reynolds number. An integral energy equation enhances comprehension of the fundamental physical mechanisms. The factors contributing to convective instability in the system are clarified using this approach.

1. Introduction

Recent studies have focused on reducing viscous shear force-induced skin friction drag in fluid flow problems under various circumstances. Rough surfaces increase skin friction drag in fluids. Choi [1] contradicted this by conducting experiments on how surface

[☆] Authors are thankful to Prince Sultan University.

* Corresponding author.

E-mail addresses: sohail@qau.edu.pk (S. Nadeem), hghazwani@jazanu.edu.sa (H.A. Ghazwani).

<https://doi.org/10.1016/j.heliyon.2024.e26779>

Received 2 August 2023; Received in revised form 20 February 2024; Accepted 20 February 2024

Available online 1 March 2024

2405-8440/© 2024 The Authors. Published by Elsevier Ltd. This is an open access article under the CC BY-NC-ND license (<http://creativecommons.org/licenses/by-nc-nd/4.0/>).

roughness influences fluid flow and other factors. The study investigated rough surface phenomena and complicated dynamics and how they affect fluid behavior. Sirovich and Karlsson [2] examined passive drag reduction in a turbulent flow. They tested numerous passive drag-reduction methods. Von Kármán [3] investigated incompressible steady flow in a smooth, infinite plane rotating at a certain rotational velocity. The boundary layer's three-dimensional velocity distribution is radially inflectional. Cross-flow velocity, the third velocity component with swept wings for aircraft in boundary-layer flow is perpendicular to the other two components layer. Cross-flow boundary layers are frequent across rotating disks. The cross-flow component includes the centrifugally produced radial flow velocity, as well as azimuthal and perpendicular components. Gregory et al. [4] examined von Kármán flow stability at high Reynolds numbers. This showed boundary layer spiral vortex disturbances. A disk made of china clay was imprinted by co-rotating vortices caused by a cross-flow. Unlike swept wings, rotating disc boundary layers experience Coriolis forces (see Table 5).

Malik [5] generated the neutral curves in the boundary layer of a revolving disk with stationary instability modes. He distinguished between instabilities caused by inviscid cross-flow and those caused by viscous streamline-curvature interactions, establishing both. Boundary layer flow stability on rotating disks has been clarified by these investigations. Hall's [6] research on the two stability branches for the high limit of Reynolds number yielded strong concordance with Malik's neutral curve. The first branch (type I) represents the cross-flow instability upper branch. The lower branch which is the second branch (type II) balances Coriolis and viscous forces and streamlines curvature. Since type I is theoretically dominant, this type is hard to verify experimentally.

Watanabe et al. [7] described von Kármán's laminar-turbulent transition. The literature provides two von Kármán flow surface roughness models. Yoon et al. [8] the first model simulates concentric grooved radially anisotropic roughness. For Miklavčič and Wang's [9] MW model no-slip boundary condition is replaced by the partial-slip boundary condition for empirical prediction of surface roughness. Adjusting radial and azimuthal boundary conditions models roughness separately. MW models roughness. Isotropic roughness, concentric, and radial grooves. Cooper et al. [10] investigated whether distributed surface roughness might affect instability in the MW formulation rotating disk system. Convective stability analysis stabilizes Type I mode. If the concentric grooves are anisotropically rough, the Type II mode can become unstable. Two roughness models predicted stability for Garrett et al. [11]. MW and YHP affected Type I and II modes differently. Roughness reduces YHP Reynolds-stress energy.

Rotating disc magnetohydrodynamic fluid flow is used in turbomachinery, computer disc drives, geophysical fluid dynamics, nuclear reactors and gaseous, MHD power producers, flow meters, pumps, and other things. Chemical vapor deposition reactors with a rotating disc flow put electrical and optical materials on surfaces used in electrochemistry. For additional deposition, these reactors need laminar gas flow near the top. In this study, the breakdown of the laminar boundary layer, direct temporal resonance, direct spatial resonance, and absolute instability are all investigated. On a rotating disk immersed in a circular magnetic field, Pao [12] investigated the flow of an incompressible viscous conducting fluid. Magnetic fields thicken flow boundary layers and reduce axial flowfields. Furthermore, High magnetic fields separate the boundary layer from the disk surface.

Jasmine et al. [13] discussed rotating disk boundary layer stability under a uniform axial magnetic field. The magnetic field considerably stabilizes flow, and linear stability theory predicts absolute instability. In Turkyilmazoglu's [14] later study, the vertical magnetic field considerably decreases absolute instability and all resonance mechanisms in linear stability theory. Direct spatial resonance was the most dangerous one. The stability and roughness of a rotating disk are both affected by nanoparticles. Fluid properties, disk stability, and surface roughness are all affected by nanoparticles. The fluid flow around the rotating disk is influenced by the size, shape, and concentration of the nanoparticles. Nanoparticles increase the viscosity of the fluid, which stabilizes the discs. Turbulence is caused by larger nanoparticle clusters. The roughness of a rotating disk can be modified using nanoparticles. Choi's "nanofluids" enhanced the fluid dynamics of nanoparticles. The advantages of nanofluids are questioned in practical applications. Nanofluids are discussed by Wang and Mujumdar [15] and Wong and Leon [16]. Restricted nanofluids. Researchers like Bachok et al. [17,18], Grosan and Pop [19], Yacob et al. [20], and others looked at nanofluids in Newtonian and porous media with both stationary and dynamic boundaries. Boundary layer transport is observed in nanofluids. Wang et al. [23] investigated how a melting heat transmission mechanism affects the 3D flow of non-Newtonian nanofluid along the stretched sheet. Wang et al. [24,25] studied the activation energy on non-Newtonian liquid and which involve chemical reactions. He also worked on non-Newtonian liquid based on Prabhakar's fractional derivative with generalized Fourier's law. The results were statistically analyzed using the shooting method and Laplace transformation technique, respectively. Research on nanofluids using MHD slip flow. The MHD slip flow and magnetic field-nanoparticle interactions are modified by the presence of nanofluids. Nanofluid boundary layer behavior, MHD slip flow, and applications are all discussed in these works.

The linear convective instability for an enforced axial flow with MHD of nanofluid in isotropic and anisotropic surface roughness resulting over a rough rotating disk in boundary layer flow will be examined in this work. The steady mean flow involving the magnetic field of nanofluid is governed. The equations for the rotating disk are presented in Section 2, utilizing the MW model for the magnetic field of nanofluid with enforced axial flow. The resulting stable flows' of two sets of linear stability characteristics are examined in Section 3. In Section 4, linear amplification rates are investigated for the strength of magnetic fields and volume fraction of nanoparticles functioning in the unstable field using numerical analysis. In Section 5, we expand the base flow's slip-velocity roughness model to include perturbations. In Section 6, We use the perturbed system to extract the relevant equations and energy analyses conduction of the magnetic field and nanoparticles with the axial flows in anisotropic roughness and isotropic roughness for specific disturbance eigenmodes. In Section 7, we examine and summarize our results.

2. Mathematical formulation

This section investigates the behavior of a rotating disk submerged in an electrically conducting incompressible fluid containing nanoparticles over an infinite disk rotating at a constant angular velocity Ω^* about its axis of rotation z^* and the effect of surface roughness

(See Fig. 1). A uniform magnetic field $B = B_0$ is assumed to be applied perpendicular to the surface of the rough disk. In this section, we will discuss how the magnetic field affects the hydrodynamic properties for fluid motion, specifically in relation to the momentum equation. This effect can be observed in the form of $\mathbf{J} \times \mathbf{B}$ in the momentum equation. The Lorentz force refers to the combination of electric and magnetic forces acting on a charged particle. The force has components that can be evaluated as $(-u, -v, 0)$ for a normal electric field. The fluid is entrained towards the disk's surface and flows with velocity $U = (u^*, v^*, w^*)$, where r^* , θ , and z^* stand for radial, azimuthal, and axial velocities, respectively. An $*$ denotes a dimensional quantity. The cylindrical polar coordinates form of the Navier-Stokes equations for flow exterior to the boundary layer in the rotating frame of reference are

$$\nabla^* \cdot U^* = 0 \tag{2.1}$$

$$\left(\frac{\partial}{\partial t^*} + U^* \cdot \nabla^* \right) U^* + 2\Omega \times U^* + \Omega \times (\Omega \times r^*) = -\frac{1}{\rho_{nf}^*} \nabla^* \cdot p^* + \frac{1}{\rho_{nf}^*} \nabla^* \cdot \tau^* + \frac{1}{\rho_{nf}^*} \mathbf{J} \times \mathbf{B} \tag{2.2}$$

$$\left(\rho^* C_p^* \right)_{nf} \left(\frac{\partial}{\partial t^*} + U^* \cdot \nabla^* \right) T^* = k_{nf}^* \nabla^{*2} T^* \tag{2.3}$$

Here, t^* stands for time, r^* for radial position vector in space, p for fluid pressure, C_p^* stands for specific heat capacity and constant angular velocity is $\Omega = (0, 0, \Omega)$. For generalized Newtonian models $\tau^* = \mu^* \dot{\gamma}^*$ represents the stress tensor, where μ^* stands for constant viscosity and the strain tensor's rate is $\dot{\gamma}^* = \nabla^* U^* + \nabla^{*T} (U^*)^T$.

Now to derive disk surface boundary condition for surface roughness we apply the MW model [9]. According to this method, partial-slip conditions rather than no-slip conditions can be used to simulate roughness at the disk surface. The Navier-Stokes equation includes a generalisation of partial-slip conditions in its radial and azimuthal direction respectively

$$u^*(0) = M_1 \rho_{nf}^* \mu_{nf}^* \frac{\partial u^*}{\partial z^*}(0) \tag{2.4}$$

$$v^*(0) = M_2 \rho_{nf}^* \mu_{nf}^* \frac{\partial v^*}{\partial z^*}(0) \tag{2.5}$$

Where ρ_{nf}^* is the nanofluid density and μ_{nf}^* is the nanofluid dynamics viscosity, which are then provided by

$$\mu_{nf}^* = \frac{\mu_f^*}{(1-\varphi)^{(2.5)}} \rho_{nf}^* = (1-\varphi) + \varphi \left(\frac{\rho_s^*}{\rho_f^*} \right)$$

where the solid and liquid fractions' densities are shown by ρ_s^* and ρ_f^* , and the nanoparticle's viscosity of the fluid fraction is shown by μ_f^* .

Let $\lambda = M_1 \rho_f^* \sqrt{\mu_f^* \Omega^*}$ and $\eta = M_2 \rho_f^* \sqrt{\mu_f^* \Omega^*}$, where M_1 and M_2 refer to the corresponding slip coefficients that are determined through experimentation.

Now $u^*(0) = AB\lambda \frac{\partial u^*}{\partial z^*}(0)$, and $v^*(0) = AB\eta \frac{\partial v^*}{\partial z^*}(0)$, where $A = \frac{\rho_{nf}^*}{\rho_f^*} = (1-\varphi) + \varphi \left(\frac{\rho_s^*}{\rho_f^*} \right)$ and $B = \frac{\mu_{nf}^*}{\mu_f^*} = \frac{1}{(1-\varphi)^{(2.5)}}$.

The scaling variables non-dimensionalize the governing equations Al-Malki [21] and express them in cylindrical polar coordinates.

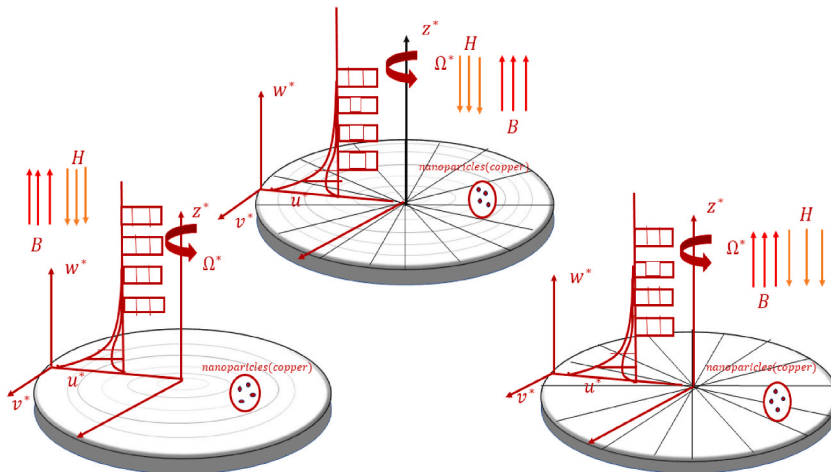


Fig. 1. Rotating disk with MHD and nanoparticles in anisotropic and isotropic roughness.

$$U^* = (u, v, \delta w)U_\infty^*, (r^*, z^*) = (r, \delta z)L^*, p^* = p(U_\infty^*)^2 \rho^*,$$

$$t^* = t \left(\frac{L^*}{U_\infty^*} \right), T^* - T_\infty^* = T(T_w^* - T_\infty^*) \tag{2.6}$$

Here, the free stream velocity is defined by $U_\infty^* = L^* \Omega^*$, the boundary layer scaling constant is defined by δ , and the general length scale is defined by L^* . Since the laminar flow is axisymmetric and steady, all derivatives concerning t are neglected. $Re = \frac{U_\infty^* L^* \rho_f^*}{\mu_f^*}$ is used to define Reynolds number.

These lead to the governing non-dimensional equations as follows:

$$\frac{1}{r} \frac{\partial ru}{\partial r} + \frac{\partial w}{\partial z} = 0, \tag{2.7}$$

$$u \frac{\partial u}{\partial r} + w \frac{\partial u}{\partial z} - \frac{(v+1)^2}{r} = rH^2 + \frac{B}{A} \frac{1}{\delta^2 Re} \left(\mu_f \frac{\partial^2 u}{\partial z^2} + \frac{\partial \mu_f}{\partial z} \frac{\partial u}{\partial z} \right) - \frac{M}{A} u \tag{2.8}$$

$$u \frac{\partial v}{\partial r} + w \frac{\partial v}{\partial z} - \frac{(uv)}{r} + 2u = \frac{B}{A} \frac{1}{\delta^2 Re} \left(\mu_f \frac{\partial^2 v}{\partial z^2} + \frac{\partial \mu_f}{\partial z} \frac{\partial v}{\partial z} \right) - \frac{M}{A} v \tag{2.9}$$

$$u \frac{\partial w}{\partial r} + w \frac{\partial w}{\partial z} = -\frac{1}{\delta^2} \frac{\partial p}{\partial z} + \frac{B}{A} \frac{1}{\delta^2 Re} \left(\mu_f \frac{\partial^2 w}{\partial z^2} + 2 \frac{\partial \mu_f}{\partial z} \frac{\partial w}{\partial z} \right) \tag{2.10}$$

$$u \frac{\partial T}{\partial r} + w \frac{\partial T}{\partial z} = \frac{C}{\delta^2 Re Pr} \left(\frac{\partial^2 T}{\partial z^2} \right) \tag{2.11}$$

where $M = \frac{\sigma B_0^2}{\rho_f \Omega}$ is the magnetic field parameter. Prandtl number is defined as $Pr = \frac{C_p \mu_{sf}^*}{k_f^*}$ where $C = \frac{k_{nf}}{k_f} = \frac{(k_s + 2k_f) - 2\phi(k_f - k_s)}{(k_s + 2k_f) + \phi(k_f - k_s)}$. The symbol μ_f represents constant viscosity of fluid. The boundary-layer thickness is defined as $\delta = \sqrt{\frac{\mu_\infty^*}{\Omega^* \rho_f^*}} = \delta^* L$. A Parameter for H is the ratio between the local slip velocity and the disk surface rotating speed at a given radial position.

The self-similar solutions introduction for the derivation of the mean flow equations.

$$u = rU(Z), v = rV(Z), w = rW(Z), p = P(Z), T = \bar{\theta}(Z) \tag{2.12}$$

The steady flow formulation is in accordance with Al-Malki [21] paper and that all the necessary information regarding the data as well as the derivation for the governing equations can be noticed in that paper. It can be stated that the cylindrical polar coordinate system was utilized to work with the rotating disk in presence of MHD of nanofluid and axial flow is enforced. An ODE system can be used to express the steady mean-flow profiles

$$2U + W' = 0 \tag{2.13}$$

$$U^2 - \frac{B}{A} U' - (V+1)^2 + \frac{MU}{A} + U'W - H^2 - \frac{MH}{A} = 0 \tag{2.14}$$

$$2U(V+1) - \frac{B}{A} V' + V'W + \frac{M}{A} (V+1) = 0 \tag{2.15}$$

$$WW' + P' - \frac{B}{A} W' = 0 \tag{2.16}$$

$$W\bar{\theta}' - \frac{C}{Pr} \bar{\theta}'' = 0 \tag{2.17}$$

The boundary conditions for the ODE system (2.11)–(2.14) are defined by modifying the wall conditions using equations (2.3) and (2.4), and can be written as:

$$U(0) = AB\lambda U'(0), U(0) = AB\eta U'(0), W(0) = 0, P(0) = 0, \bar{\theta}(0) = 1 \tag{2.18}$$

$$U(z \rightarrow \infty) - H = 0 = V(z \rightarrow \infty) + 1 = \bar{\theta}(z \rightarrow \infty) \tag{2.19}$$

To illustrate the magnetic field of nanofluid in the radial and azimuthal directions, we will discuss the M and ϕ for λ and η . In the case where $\lambda = 0$ and $\eta = 0$, the boundary conditions simplify the concept of no-slip boundary conditions for disk with a smooth surface. We will discuss the concept of magnetic field and volume fractions of nanoparticles with anisotropic and isotropic roughness. An example of anisotropic roughness is concentric grooves with $\eta = 0.25$ and $\lambda = 0$ while radial grooves have $\eta = 0$ and $\lambda = 0.25$. On

the other hand, isotropic roughness occurs when $\lambda = \eta = 0.25$.

2.1. Mean-flow results

2.1.1. Effects of M and volume fraction of nanoparticles ϕ with azimuthally-anisotropic roughness $\lambda = 0.25, \eta = 0$

In Fig. 2, we have obtained the mean-flow solutions by increasing the range of volume fraction of nanoparticles ϕ and magnetic field M with different ranges of enforced axial flow H over the azimuthally-anisotropic roughness $\lambda = 0.25$ and $\eta = 0$ and observed their influence w.r.t enforced axial flow. In Fig. 2(a), we observed that the change in the boundary layer thickness is very slight, as we increase the strength of magnetic field M for the different axial flow strength H , which is also increasing, the Lorentz force creates the resistance for flow in U -profiles for M and the radial jets decrease. In Fig. 2(a1) we see that as we increase the value of ϕ in the ranges of H the maximum of the U profile of ϕ increases. When both ϕ and axial flow strengths are increased, higher radial jets are produced, but the characteristic inflection is repressed. Furthermore, it can be noted that increasing the value of H results in the axial direction by showing increased behavior of component U . The highest value of U is observed close to the wall. The boundary condition refers to the point at which the profiles cover a shorter distance, indicating a gradual reduction in the boundary layer due to the impacts of presence of solid nanoparticles. In Fig. 2(b) where V is the azimuthal velocity for the effect of magnetic field M variations in radial grooves. The V -profiles in presence of the magnetic field are close to the disk of the surface and Lorentz force resistance is involved in it. Fig. 2(b1) shows that an increase in range of H and the volume fraction of nanoparticles and make the boundary layer flow thinner. In Fig. 2(c) the movement of the axial profile is away from the disk surface. It shows the unbounded behavior of the axial profile when we increase the magnetic field M and the distance from the disk increases. Fig. 2(c1) shows similar behavior to that of Fig. 2(c) for increasing the value of ϕ .

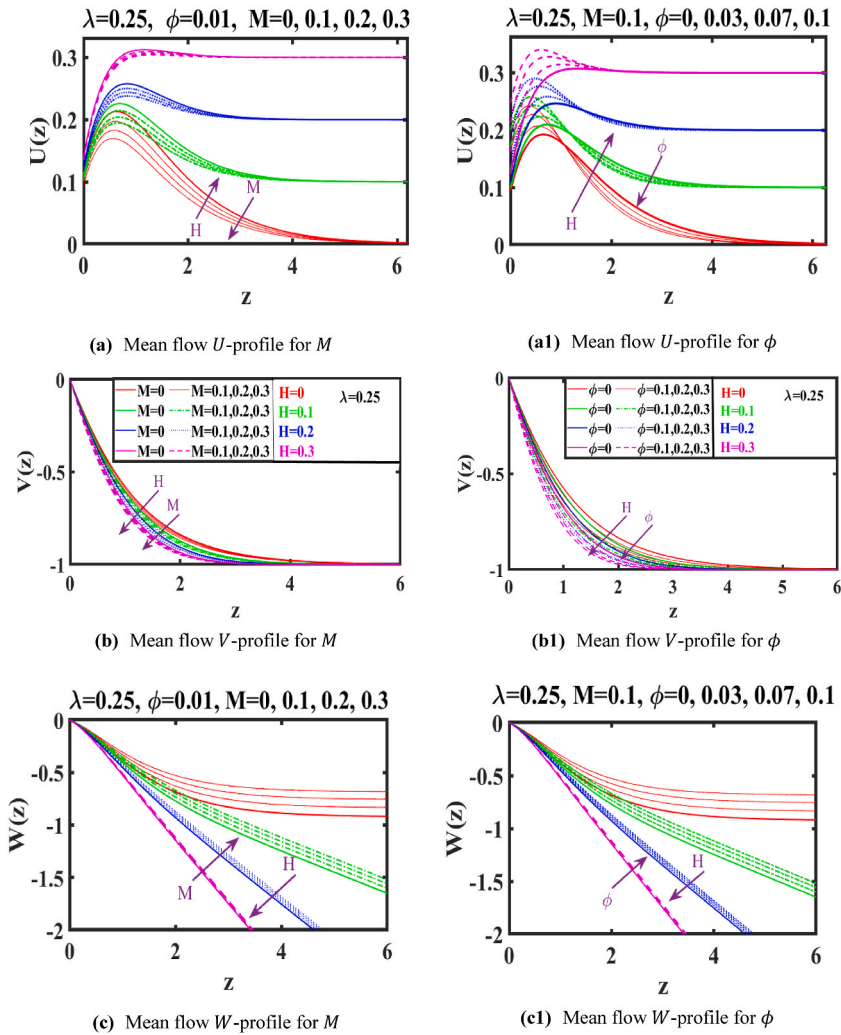


Fig. 2. Azimuthally-anisotropic roughness, Mean flow U, V, W -profiles for M and ϕ with range of H , red solid lines (—) for $H = 0$, green dashed-dotted lines (-.-) for $H = 0.2$, pink dashed lines (- -) for $H = 0.3$.

2.1.2. Effects of M and volume fraction of nanoparticles ϕ with the radially-anisotropic roughness $\lambda = 0$, $\eta = 0.25$

In Fig. 3, we have obtained the mean-flow solutions of different values of the magnetic field M and ϕ for ranges of H over the radially-anisotropic roughness for $\lambda = 0$ and taking $\eta = 0.25$. Fig. 3(a) and (a1) show the similar behavior as 2(a) for both the magnetic field and ϕ . Fig. 3(b) shows the behavior as 2(b) for the magnetic field. Fig. 3(b1) shows that as increased the values of ϕ , this drop in the V -profile for volume fraction of nanoparticles wall value. Fig. 3(c) and (c1) shows the same behavior as Fig. 2(c) by increasing the strength of magnetic field and the volume fraction of nanoparticles.

2.1.3. Effects of M and volume fraction of nanoparticles ϕ with isotropic roughness $\lambda = 0.25$, $\eta = 0.25$

In Fig. 4, we have obtained the mean-flow solutions of different values of the magnetic field M and ϕ for ranges of H over the isotropic roughness $\lambda = 0.25$ and $\eta = 0.25$. Fig. 4(a) show the behavior as Fig. 2(a) for the magnetic field. As shown in Fig. 3(a1), for the isotropically rough disk $U(z)$ profiles are slightly different. Here, the results definitely indicate that a mild increase in the radial wall jet by increasing the range of ϕ and an overall thinning effect will occur. Fig. 4(b and c) shows the same behavior as 2 (b, c) and 3 (b, c) for the magnetic field and for the values of ϕ . Fig. 4(c1) is the combination for Fig. 3(c) and also it acts as moving towards the disk surface.

Fig. 4(d) shows that for the concentric grooves of the temperature profile for the range of volume fraction of nanoparticles with axial flow fixed at $H = 0.1$ are very closed to the disk surface and increasing the value of ϕ enhanced the thermal conductivity, so the temperature increased. In the isotropic grooves, the boundary layers became thinner. The slightly drop in the wall value for the radially roughness.

Table 1 gives the values of the mean flow solution for the range of magnetic field and volume fractions of nanoparticles with

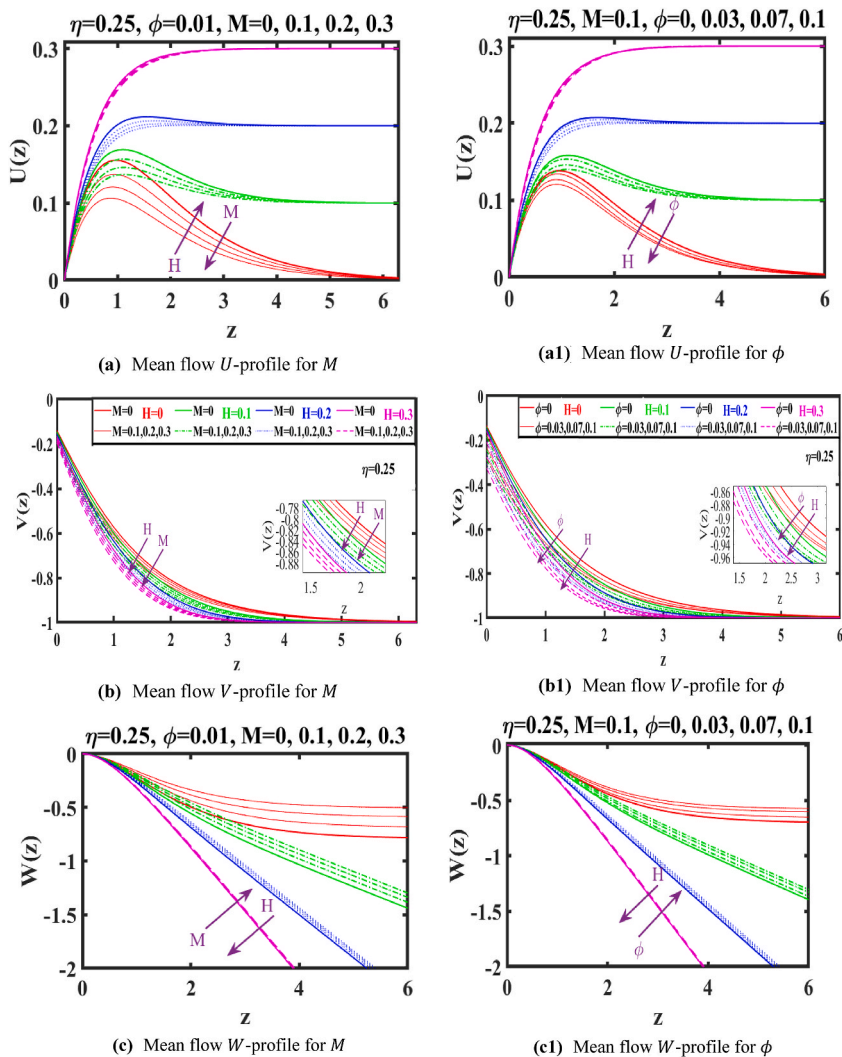


Fig. 3. Radially-anisotropic roughness, Mean flow U , V , W -profiles for M and ϕ with range of H , red solid lines (—) for $H = 0$, green dashed-dotted lines (— · —) for $H = 0.1$, blue dotted lines (····) for $H = 0.1$, blue dotted lines (····) for $H = 0.2$, pink dashed lines (— · —) for $H = 0.3$.

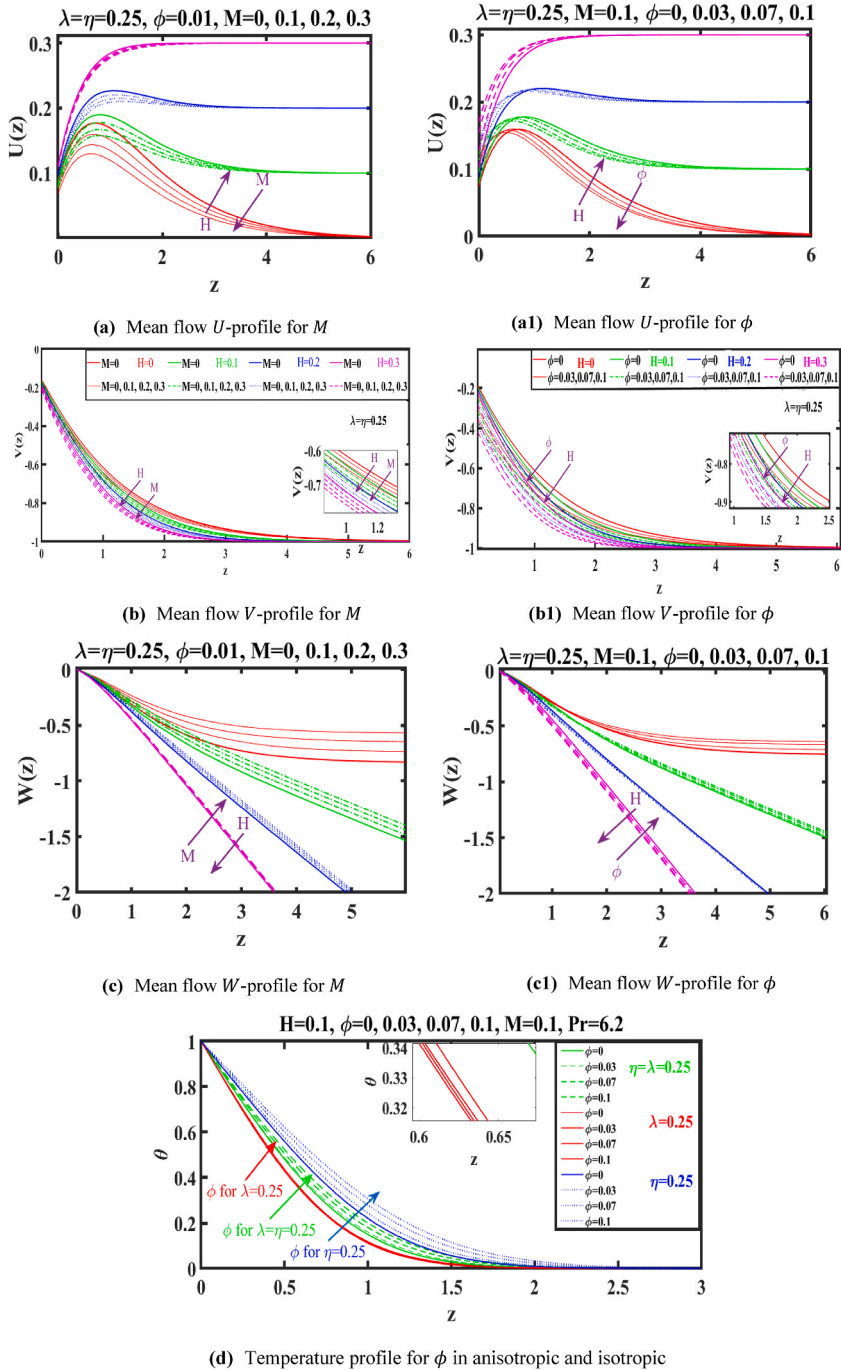


Fig. 4. Isotropic roughness, Mean flow U, V, W -profiles for M and ϕ with range of H , red solid lines (—) for $H = 0$, green dashed-dotted lines (— · —) for $H = 0.1$, blue dotted lines (····) for $H = 0.2$, pink dashed lines (— · —) for $H = 0.3$.

anisotropic and isotropic roughness. The results also contains the effect of H for its different values. When fixing the value of $H = 0, 0.1, 0.2, 0.3$ the results shows the means flow behavior and values of M and ϕ . Table 2 shows the temperature profile data for range of nanoparticles with the presence of magnetic field when the axial flow is $H = 0.1$.

3. Convective instability

On the steady mean-flow system, there will be an analysis of the local linear instability carried out. Here, we examine how a magnetic field affects the convective instability of hydromagnetic rotating disk flows. According to Refs. [7,10], the perturbation

Table 1
Mean Flow Data of M and φ for variable axial Flow H with Anisotropic and Isotropic Roughness.

λ	η	H	φ	M	$U(0)$	$V(0)$	M	φ	$U(0)$	$V(0)$
0.25	0	0	0.01	0	0.4002	-0.7551	0.1	0	0.3776	-0.7630
				0.1	0.3778	-0.7904		0.03	0.3735	-0.8422
				0.2	0.3570	-0.8263		0.07	0.3511	-0.9330
				0.3	0.3379	-0.8235		0.1	0.3269	-0.9895
		0.1	0	0.4132	-0.7892	0	0.3977	-0.8008		
			0.1	0.3976	-0.8295	0.03	0.3926	-0.8837		
			0.2	0.3834	-0.8698	0.07	0.3687	0.9789		
			0.3	0.3705	-0.9100	0.1	0.3433	-1.0382		
		0.2	0	0.4467	-0.8418	0	0.4377	0.8537		
			0.1	0.4372	-0.8844	0.03	0.4312	-0.9427		
			0.2	0.4288	-0.9265	0.07	0.4044	-1.0448		
			0.3	0.4213	-0.9680	0.1	0.3763	-1.1081		
	0.3	0	0.4994	-0.9056	0	0.4959	-0.9154			
		0.1	0.4950	-0.9488	-	0.03	0.4876	-1.0121		
		0.2	0.4913	-0.9912	-	0.07	0.4565	-1.1226		
		0.3	0.4883	-1.0326	0.1	0.4242	-1.1909			
	0.25	0	0.01	0	0.4177	-0.5043	0	0.3831	-0.5388	
				0.1	0.3851	-0.5369	0.03	0.3849	-0.5291	
				0.2	0.3553	-0.5696	0.07	0.3709	-0.5005	
				0.3	0.3281	-0.6020	0.1	0.3528	-0.4717	
		0.1	0	0.4271	-0.5260	0	0.4026	-0.5639		
			0.1	0.4042	-0.5618	0.03	0.4030	-0.5534		
			0.2	0.3840	-0.5967	0.07	0.3874	-0.5233		
			0.3	0.3664	-0.6306	0.1	0.3682	-0.4931		
		0.2	0	0.4621	-0.5602	0	0.4471	-0.5987		
			0.1	0.4489	-0.5966	0.03	0.4482	-0.5877		
			0.2	0.4381	-0.6314	0.07	0.4333	-0.5558		
			0.3	0.4293	-0.6648	0.1	0.4146	-0.5238		
	0.3	0	0.5234	-0.6355	0	0.5160	-0.6376			
		0.1	0.5190	-0.6355	0.03	0.5204	-0.6261			
		0.2	0.5164	-0.6690	0.07	0.5091	-0.5918			
		0.3	0.5152	-0.7010	0.1	0.4927	-0.5573			
	0.25	0.25	0	0.01	0	0.4002	-0.7551	0	0.2979	-0.5989
					0.1	0.3778	-0.7904	0.03	0.2721	-0.6001
					0.2	0.2680	-0.6272	0.07	0.2288	-0.2694
					0.3	0.2475	-0.6535	0.1	0.1959	-0.5474
0.1			0	0.3250	-0.6012	0	0.3159	-0.6278		
			0.1	0.3079	-0.6302	0.03	0.2885	-0.6287		
			0.2	0.2925	-0.6590	0.07	0.2436	-0.6045		
			0.3	0.2789	-0.6873	0.1	0.2094	-0.5733		
0.2			0	0.3562	-0.6404	0	0.3544	-0.6680		
			0.1	0.3459	-0.6707	0.03	0.3256	-0.6692		
			0.2	0.3370	-0.7001	0.07	0.2784	-0.6435		
			0.3	0.3294	-0.7285	0.1	0.2425	-0.6102		
0.3	0	0.4078	-0.6869	0	0.4121	-0.1736				
	0.1	0.4033	-0.7166	0.03	0.3821	-0.7150				
	0.2	0.3998	-0.7452	0.07	0.3321	-0.6871				
	0.3	0.3971	-0.7726	0.1	0.2935	-0.6509				

Table 2
Temperature profile Data for $M = 0.1$ with Anisotropic and Isotropic Roughness at fixed axial Flow $H = 0.1$.

λ	η	φ	$-\bar{\theta}(0)$	λ	η	$-\bar{\theta}(0)$	λ	η	$-\bar{\theta}(0)$
0.25	0	0	1.1048	0	0.25	1.2121	0.25	0.25	0.9037
		0.03	1.0909			1.2390			0.8660
		0.07	1.0517			1.2536			0.8106
		0.1	1.0127			1.2520			0.7681

equations are not effective by the partial-slip boundary conditions. This means that the surface roughness have no affected on the governing stability equations in the MW model. The MHD nanofluid perturbation equations are used and we offer the entire derivation of those equations. In order to get the perturbation equations for the magnetic field M and φ , we make use of the system presented in Equation (2.2). When compact disturbances are applied to the steady-mean flow, they are introduced at a particular radius, and the local Reynolds number is defined as $R = \frac{r_s^2 \Omega^2 \sigma \rho_f^*}{\mu_\infty}$. These equations are non-dimensionalised, Al-Malki [21], by using the following scales for new velocity, length, pressure and time

$$(r^*, z^*) = (r, z)\delta^*, U^* = (u, v, \delta w)r_s^* \Omega^*, p^* = p(r_s^* \Omega^*)^2 \rho^*,$$

$$t^* = t \left(\frac{L^*}{r_s^* \Omega^*} \right), T^* - T_\infty = T(T_w^* - T_\infty^*) \tag{3.1}$$

$$u(r, \theta, z, t) = \frac{r}{R} U(z) + \check{u}(r, \theta, z, t) \tag{3.2}$$

$$v(r, \theta, z, t) = \frac{r}{R} V(z) + \check{v}(r, \theta, z, t) \tag{3.3}$$

$$w(r, \theta, z, t) = \frac{1}{R} W(z) + \check{w}(r, \theta, z, t) \tag{3.4}$$

$$T(r, \theta, z, t) = \bar{\theta}(z) + \check{\theta}(r, \theta, z, t) \tag{3.5}$$

$$p(r, \theta, z, t) = \frac{1}{R^2} P(z) + \check{p}(r, \theta, z, t) \tag{3.6}$$

This leads to the following equation of the instantaneous non-dimensional pressure and velocities components

$$\frac{\partial \check{u}}{\partial r} + \frac{\check{u}}{r} + \frac{1}{r} \frac{\partial \check{v}}{\partial \theta} + \frac{\partial \check{w}}{\partial z} = 0, \tag{3.7}$$

$$\frac{\partial \check{u}}{\partial t} + \frac{rU}{R} \frac{\partial \check{u}}{\partial r} + \frac{U\check{u}}{R} + \frac{V}{R} \frac{\partial \check{u}}{\partial \theta} + \frac{W}{R} \frac{\partial \check{u}}{\partial z} + \frac{r\check{U}\check{w}}{R} \frac{2(V+1)\check{v}}{R} = -\frac{\partial \check{p}}{\partial \theta} + \frac{1}{R} \left(\frac{\partial^2 \check{u}}{\partial r^2} + \frac{1}{r} \frac{\partial \check{u}}{\partial r} + \frac{1}{r^2} \frac{\partial^2 \check{u}}{\partial \theta^2} + \frac{\partial^2 \check{u}}{\partial z^2} + \frac{2}{r^2} \frac{\partial \check{v}}{\partial \theta} \frac{\partial \check{u}}{\partial r} \right) \frac{1}{R} M\check{u} \tag{3.8}$$

$$\frac{\partial \check{v}}{\partial t} + \frac{rU}{R} \frac{\partial \check{v}}{\partial r} + \frac{U\check{v}}{R} + \frac{V}{R} \frac{\partial \check{v}}{\partial \theta} + \frac{W}{R} \frac{\partial \check{v}}{\partial z} + \frac{r\check{V}\check{w}}{R} + \frac{2(V+1)\check{u}}{R} = -\frac{1}{r} \frac{\partial \check{p}}{\partial \theta} + \frac{1}{R} \left(\frac{\partial^2 \check{v}}{\partial r^2} + \frac{1}{r} \frac{\partial \check{v}}{\partial r} + \frac{1}{r^2} \frac{\partial^2 \check{v}}{\partial \theta^2} + \frac{\partial^2 \check{v}}{\partial z^2} + \frac{2}{r^2} \frac{\partial^2 \check{u}}{\partial \theta} \frac{\partial \check{v}}{\partial r} \right) \frac{1}{R} M\check{v} \tag{3.9}$$

$$\frac{\partial \check{w}}{\partial t} + \frac{rU}{R} \frac{\partial \check{w}}{\partial r} + \frac{W}{R} \frac{\partial \check{w}}{\partial \theta} + \frac{W}{R} \frac{\partial \check{w}}{\partial z} + \frac{W\check{w}\check{w}}{R} = -\frac{\partial \check{p}}{\partial z} + \frac{1}{R} \left(\frac{\partial^2 \check{w}}{\partial r^2} + \frac{1}{r} \frac{\partial \check{w}}{\partial r} + \frac{1}{r^2} \frac{\partial^2 \check{w}}{\partial \theta^2} + \frac{\partial^2 \check{w}}{\partial z^2} \right) \tag{3.10}$$

$$\frac{\partial \check{\theta}}{\partial t} + \frac{rU}{R} \frac{\partial \check{\theta}}{\partial r} + \frac{W}{R} \frac{\partial \check{\theta}}{\partial \theta} + \frac{W}{R} \frac{\partial \check{\theta}}{\partial z} + \bar{\theta}\check{w} = \frac{1}{RP_r} \left(\frac{\partial^2 \check{\theta}}{\partial r^2} + \frac{1}{r} \frac{\partial \check{\theta}}{\partial r} + \frac{1}{r^2} \frac{\partial^2 \check{\theta}}{\partial \theta^2} + \frac{\partial^2 \check{\theta}}{\partial z^2} \right) \tag{3.11}$$

To show the stability equations in separable form as r, θ and t use the perturbation quantities in normal mode, which gives the following:

$$(\check{u}, \check{v}, \check{w}, \check{p}) = (\hat{u}, \hat{v}, \hat{w}, \hat{p}, \hat{\theta}) e^{i(\alpha r + n\theta - \omega t)} \tag{3.12}$$

where hat-marked variables are z-dependent perturbation eigenfunctions. Complex radial wavenumber $\alpha = \alpha_r + i\alpha_i$. Where $n = \beta R$ denotes the azimuthal wavenumber that is the disk's vortices in integer form. Frequency is ω .

$$i\alpha \hat{u} + \frac{\hat{u}}{R} + i\beta \hat{v} + \hat{w}' = 0 \tag{3.13}$$

$$\begin{aligned} i\omega \hat{u} + i\alpha U \hat{u} + \frac{U \hat{u}}{R} + i\beta V \hat{u} + \frac{W \hat{u}'}{R} + U' \hat{w} - \frac{2(V+1)\hat{v}}{R} = \\ -i\alpha \hat{p} + \frac{1}{R} (-\alpha^2 \hat{u} - \beta^2 \hat{u} + \hat{u}'' - M \hat{u}) \end{aligned} \tag{3.14}$$

$$\begin{aligned} i\omega \hat{v} + i\alpha U \hat{v} + \frac{\hat{v}}{R} + i\beta V \hat{v} + \frac{W \hat{v}'}{R} + V' \hat{w} + \frac{2(V+1)\hat{u}}{R} = \\ -i\beta \hat{p} + \frac{1}{R} (-\alpha^2 \hat{v} - \beta^2 \hat{v} + \hat{v}'' - M \hat{v}) \end{aligned} \tag{3.15}$$

$$i\omega \hat{w} + i\alpha U \hat{w} + \frac{W \hat{w}}{R} + i\beta V \hat{w} + \frac{W \hat{w}'}{R} = -i\hat{p} + \frac{1}{R} (-\alpha^2 \hat{w} - \beta^2 \hat{w} + \hat{w}'') \tag{3.16}$$

$$i\omega\widehat{\theta} + i\alpha U\widehat{\theta} + \frac{W\widehat{\theta}}{R} + i\beta V\widehat{\theta} + W\widehat{\theta} = \frac{1}{RP_r} (-\alpha^2\widehat{\theta} - \beta^2\widehat{\theta} + \widehat{\theta}) \tag{3.17}$$

The quadratic eigenvalue problem $(A_2\alpha^2 + A_1\alpha + A_0)\widehat{Q} = 0$ can solve system (3.13)–(3.17). The matrices A_j contain the coefficients of the $O(\alpha^j)$ terms, and H is the vector of eigenfunctions. We set $\widehat{\omega} = 0$ to concentrate on stationary vortices that rotate, within the rotating reference frame, with the rough disk.

According to Equation (3.10), it can be assumed that the first derivative of $\widehat{\omega}$ with respect to the disk surface must be equal to zero. To contain disturbances within the boundary layer, all perturbation values are set to zero at the physical domain’s far end. These are facts correspond to Cooper et al. [10]. By enforcing restrictions on small perturbations within the boundary layer, the eigenfunctions were approximated with precision while following to the boundary conditions.

$$\widehat{u}(\mathbf{0}) = \widehat{v}(\mathbf{0}) = \widehat{w}(\mathbf{0}) = \widehat{w}'(\mathbf{0}) = \widehat{\theta}(\mathbf{0}) = \mathbf{0}, z = \mathbf{0} \tag{3.18}$$

$$\widehat{u}(\infty) = \widehat{v}(\infty) = \widehat{w}(\infty) = \widehat{p}(\infty) = \widehat{\theta}(\infty), z \rightarrow \infty \tag{3.19}$$

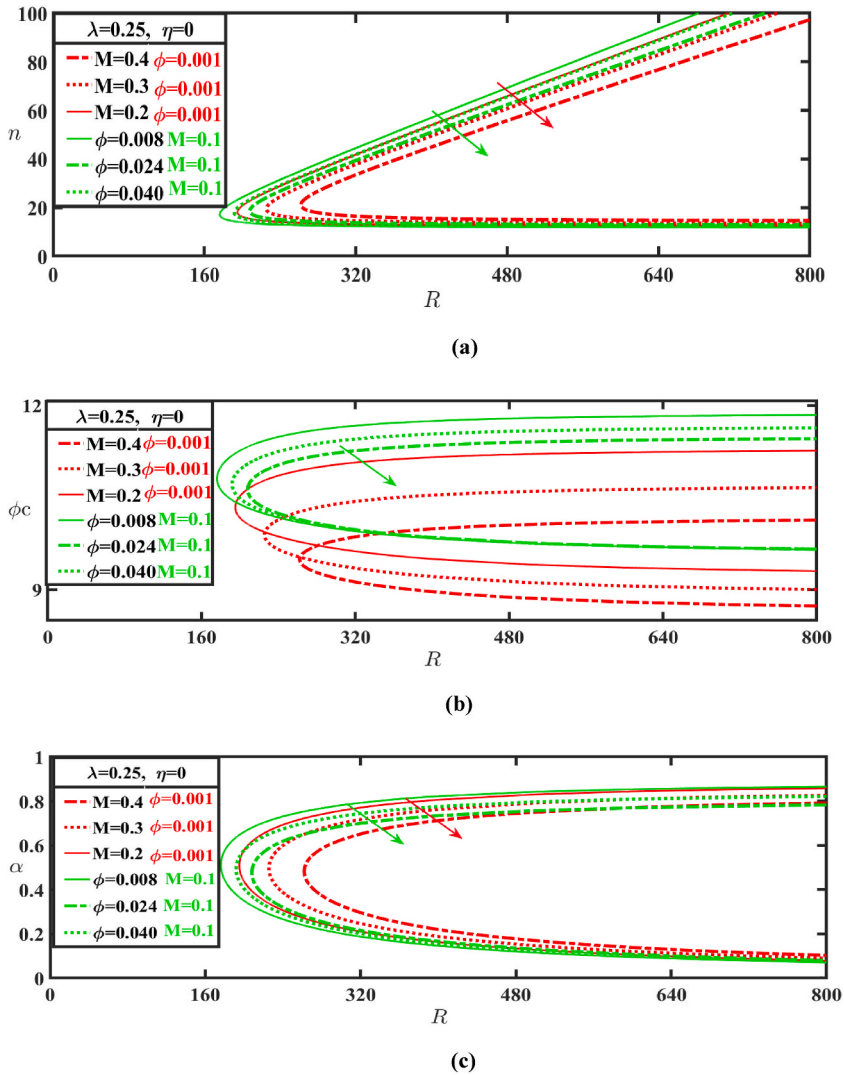


Fig. 5. Neutral stability curves of (a) vortex-number, (b) angle and (c) wavenumber for a range of M and ϕ at $H = 0.1$ with anisotropic $\lambda = 0.25, \eta = 0$ (concentric grooves).

4. Neutral stability curves results

Chebyshev polynomial discretization yields spatial stability and neutral temporal solutions. An exponential map is used to convert Gauss-Lobatto collocation points are into physical domains. The method used to solve the stability equations involves using primitive variables and collocation points that are set between the lower and upper bounds, except for the boundary conditions in Eqs. (3.18)–(3.19), which are enforced at $z = 0$ and $z = z_{max}$. Alverog lu [22]. describes the numerical method used here.

The magnetic field of nanofluid with the rough surfaces have been used to generate neutral curves, which are characterized by $\alpha^i = 0$ neutral spatial growth. These curves have been used to describe several distinct types of solutions from equations (3.13)–(3.16) with magnetic fields nanofluid. The Type I mode in neutral curves can be seen as the top lobe and it is because of the mean-flow components of the MHD and φ and their inviscid behavior. The Type II mode, which emerges as a smaller lower lobe, results from the Coriolis and streamline curvature influences. This mode is eliminated for these mean-flow components. Fig. 5 shows neutral curves from our analyses, and Table 3 shows essential Reynolds numbers for instability (see Table 4).

Fig. 5 demonstrates that the Type I mode exhibits predominant influence on the MHD boundary layers of nanofluid stability over azimuthally-anisotropic and isotropic rough surfaces, this is seen from the single-lobed shape of the boundary layers. According to the results in Table 3, more increment in M and φ and raising the critical Reynolds number can makes the boundary layer more stable.

In Fig. 5(a) When magnetic field M and φ acquires higher values the critical Reynolds number is shown to slightly increase and the inviscid type I modes are stabilized in the azimuthally-anisotropic roughness. In this instance, it can be observed that a rather little increase in the range of magnetic field M and φ totally eliminates the viscous type II mode lobe. Additionally, the value of n is greatly raised, For a variety of magnetic field and volume fraction of nanoparticles and Tables (3)–(5), wavenumber critical values is predicted in the direction of r are depicted in Fig. 5 (a). The results show that all range of M and φ gradually reduce the value of α . Type II mode lobe is also eliminated in this case.

In Fig. 5(b and c), when increasing magnetic field the type I mode become more stabilize along the upper branch of neutral curves which is associated with decrease the angle φ_c and wave number α . The radially grooved disks for the magnetic field nanofluid have a steadily destabilizing impact on the type II mode. As a result, the instability region widens, when H rises it effect the type II mode start to vanish and the type I mode takes over as the typical type of instability as seen in Fig. 6(a,b,c).

Fig. 7(a,b,c) show that isotropic roughness has same effect as concentric curves on volume fraction of nanoparticles but for the magnetic field, it gives slightly more stability for type I mode for the values of n wavelength and α .

In the axial flow strength $H = 0.1$ of the concentrically grooved and isotropic surfaces increasing the range of magnetic field and volume fraction of nanoparticles increases stabilizes type I mode the most. Flows with radial grooves are the most unstable over a disk.

5. Linear amplification rate

According to Al-Malki et al. [21] investigation, as the axial flow strength is increased, the type II mode reduces in comparison to the type I mode. The type II mode is also effected by increasing range of magnetic field and volume fraction of nanoparticles, it can be decrease or vanish on a revolving disk. In other words, increasing the magnetic field in various disk roughness can fully suppress the presence or development of the type II mode.

Fig. 8 shows the linear growth rates of type I mode for magnetic field $M = 0.1$ and $\varphi = 0.001$ in concentric, radial, and isotropic grooves, the amplification rates of stationary modes can be demonstrated by observing the surface roughness with effects of magnetic field M and φ the rotating frame when $H = 0.1$. The Lorentz force and the viscous force effect on the amplification rate. In concentric grooves, as shown in Fig. 8(a), the amplification rates for M and φ are slightly reduced. Under our model, even moderate levels of M and φ for all surface roughness cause the Type II mode to vanish, hence it is not taken into consideration here. These results confirm the stabilizing role of MHD in concentric roughness discussed in Section II, while Fig. 8(b) shows higher stability for radial grooves. In accordance with Fig. 8(c), for the isotropic grooves with M and φ there is significant reduction in amplification rates. These results support the effective stabilizing effect of MHD and volume fraction of nanoparticles in isotropic roughness.

Table 3
Critical Data for M and φ at $H = 0.1$ for instability type I with $\lambda = \eta$.

$H = 0.1,$						
$\lambda =$						
$0.25,$						
$\eta = 0.25$						
M	φ	R_c	φ_c	$\alpha_{r,c}$	n_c	
0.1	0.008	199.92	9.510	0.559	18.7	
	0.024	213.90	9.435	0.543	19.3	
	0.040	227.67	9.370	0.530	19.9	
0.2	0.001	228.71	9.054	0.556	20.3	
0.3		271.37	8.629	0.544	22.4	
0.4		323.39	8.265	0.531	25.0	

Table 4
Critical Data for M and φ at $H = 0.1$ for instability type I with $\lambda = 0.25, \eta = 0$.

$H = 0.1,$ $\lambda = 0.25, \eta = 0$					
M	φ	R_c	φ_c	$\alpha_{r,c}$	n_c
0.1	0.008	176.04	10.800	0.514	17.3
	0.024	191.73	10.710	0.494	17.9
	0.040	207.89	10.624	0.479	18.7
0.2	0.001	194.99	10.339	0.510	18.2
0.3		225.51	9.889	0.498	19.6
0.4		261.88	9.490	0.485	21.2

Table 5
Critical Data for M and φ at $H = 0.1$ for instability type I with $\lambda = 0, \eta = 0.25$.

$H = 0.1, \lambda = 0$ $\eta = 0.25$					
M	φ	R_c	φ_c	$\alpha_{r,c}$	n_c
0.1	0.008	240.39	8.854	0.435	16.3
	0.024	262.77	8.804	0.419	17.1
	0.040	285.5	8.773	0.401	17.7
0.2	0.001	288.04	8.377	0.427	18.1
0.3		363.50	7.946	0.426	21.1
0.4		463.10	7.595	0.398	24.6

6. Energy analysis

The formulation of disturbance in an integral energy equation is investigated in the literature [7,8,21,22] which allow researchers to get more knowledge of its physical mechanisms. The physical mechanism with the MHD nanofluid with surface roughness is investigated in this section. The energy equations derivation began with the multiplication of the linearized momentum Equation (3.13-(3.16)) is by the disturbance values $u, v,$ and $w,$ respectively. The kinetic-energy equation for the disturbances is obtained by adding the resulting formulas.

$$\left\{ \frac{\partial}{\partial t} + U \frac{\partial}{\partial r} + \frac{V}{r} \frac{\partial}{\partial \theta} + W \frac{\partial}{\partial z} \right\} K = -\bar{u}\bar{w} \frac{\partial U}{\partial z} - \bar{v}\bar{w} \frac{\partial V}{\partial z} - \bar{w}^2 \frac{\partial W}{\partial z} - \bar{u}^2 \frac{\partial U}{\partial r} - \frac{U\bar{v}^2}{r} - \frac{M\bar{u}^2}{r} - \frac{M\bar{v}^2}{r} + \left[\frac{\partial(\bar{u}\bar{p})}{\partial r} + \frac{1}{r} \frac{\partial(\bar{v}\bar{p})}{\partial \theta} + \frac{\partial(\bar{u}\bar{p})}{r} \right] + \left[\frac{\partial(\bar{u}_j \sigma_{ij})}{\partial x_j} - \sigma_{ij} \frac{\partial(\bar{u}_j)}{\partial x_j} \right] \quad (6.1)$$

where $K = \frac{1}{2}(\bar{u}^2 + \bar{v}^2 + \bar{w}^2)$ and σ_{ij} is the viscous stress terms, $\sigma_{ij} = \frac{1}{R} \left(\frac{\partial \bar{u}_i}{\partial x_j} - \frac{\partial \bar{u}_j}{\partial x_i} \right)$.

equation (6.1) indicates summing from 1 to 3 by the repeated suffices. The governing stability equations can remove any $O\left(\frac{1}{r}\right)$ viscous terms to maintain consistency the $O\left(\frac{1}{R^2}\right)$ terms is neglected. The boundary layer is integrated over the entire time period and azimuthal mode if the perturbations are averaged over these parameters, and derivative of t and $theta$ are then removed to leave

$$\int_0^\infty \left\{ U \frac{\partial \bar{K}}{\partial r} + \frac{\partial(\bar{u}\bar{p})}{\partial r} - \frac{\partial(\bar{u}\sigma_{11} + \bar{v}\sigma_{12} + \bar{w}\sigma_{13})}{\partial r} \right\} dz = \int_0^\infty \left[\frac{-\bar{u}\bar{w} \frac{\partial U}{\partial z} - \bar{v}\bar{w} \frac{\partial V}{\partial z} - \bar{w}^2 \frac{\partial W}{\partial z}}{1} \right] dz$$

$$- \int_0^\infty \underbrace{\sigma_{ij} \frac{\partial(\bar{u}_j)}{\partial x_j}}_2 dz - \int_0^\infty \underbrace{\frac{\partial(\bar{u}\bar{p})}{r}}_3 dz + \underbrace{(\bar{v}\bar{p})_w - [\bar{u}\sigma_{31} + \bar{v}\sigma_{32} + \bar{w}\sigma_{33}]_w}_4$$

$$- \int_0^\infty \underbrace{\frac{\partial \bar{K}}{\partial z} W dz - \int_0^\infty \bar{u}^2 \frac{\partial U}{\partial r} - \int_0^\infty \frac{U\bar{v}^2}{r} dz - \int_0^\infty \frac{M\bar{u}^2}{r} dz - \int_0^\infty \frac{M\bar{v}^2}{r} dz}_5$$

Here a period-averaged quantity is denoted by an overbar denotes, such that $\overline{u\bar{v}} = \bar{u}\bar{v}^* + \bar{u}^*\bar{v}$ (complex conjugate is indicated by $*$), the quantities assessed at the wall are denoted by w subscript. The left-hand side terms of equation (6.2) can be identified as:

- (a) the average kinetic energy convected by the mean radial flow,
- (b) the work done by the perturbation pressure, and
- (c) the work done by viscous stresses across some internal boundary in the fluid. On the right-hand side, there is
- (1) the Reynolds stress energy production term,
- (2) the viscous dissipation energy removal term,

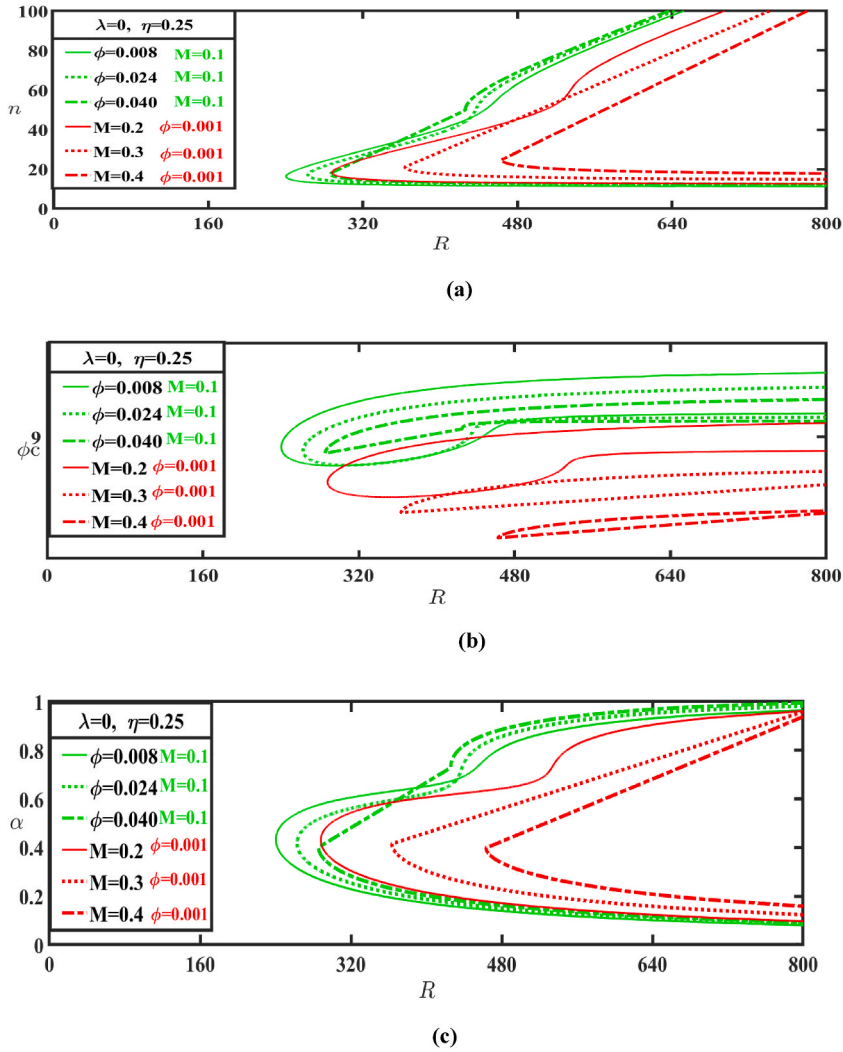


Fig. 6. Neutral stability curves of (a) vortex-number, (b) angle and (c) wavenumber for a range of M and ϕ at $H = 0.1$ with anisotropic $\lambda = 0, \eta = 0.25$ (radial grooves).

- (3) pressure work terms,
- (4) contributions from work done on the wall by viscous stresses, and
- (5) terms arising from streamline curvature effects and the three-dimensionality of the mean flow and magnetic field

The integrated mechanical energy flux is then used to normalise the energy equation, resulting in

$$-2\alpha = (P_1 + P_2 + P_3) + EDV + (PW_1 + PW_2) + (G_1 + G_2 + G_3 + G_4 + G_5) \tag{6.3}$$

Any eigenmode may be used to calculate the energy balance. The energy is added to system by the positive term while it is subtracted by the negative terms. The system spatially amplified a mode with an amplitude of ($a_j < 0$) when the energy dissipation is outweighs by the energy production. Calculating each term in the energy equation will reveal which effects of roughness are most prominent (6.3). In the energy equation, the quantities PW_2, G_1, G_2, G_3 and G_4 all negligible. The primary sources of energy generation can be identified using Reynolds stress P_2 and conventional viscous dissipation (EDV). P_1, P_3, PW_1 , and G_1 are negligible, while G_2 and G_3 are energy-draining geometric factors but for type II case they are that are significantly larger. The linear stability analysis is confirmed by the examination of energy balance.

Each component's contribution to the overall energy balance for the magnetic field M and ϕ is determined. To derive eigenfunctions for use in an energy balance analysis, we consider a variety of magnetic field strengths and nanoparticle sizes across azimuthal, axial, and isotropic roughness, all while maintaining the same axial flow rate of $R = Rc + 25$ in the type I mode. The region includes the radial position of $R = Rc + 25$ which is unstable, where the eigenfunctions are assessed at a specific Reynolds number. At this specific Reynolds number, the value of α that has been chosen represents the disturbance that goes through highest amplification.

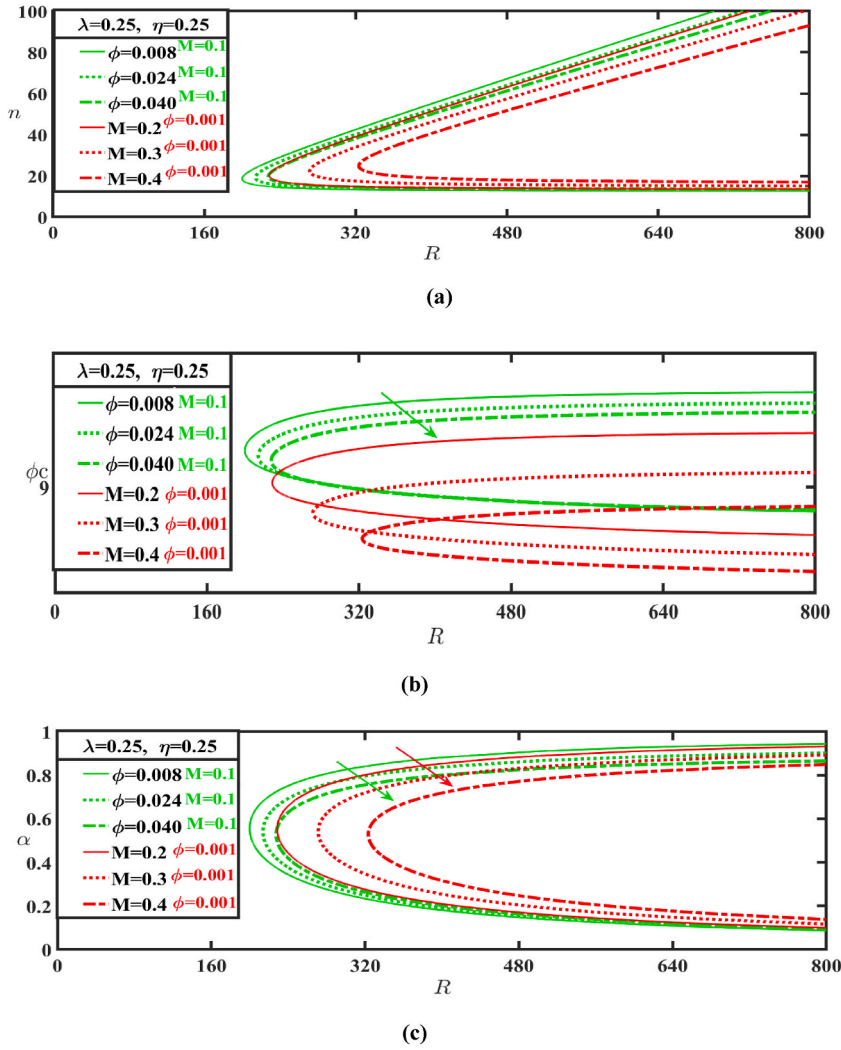


Fig. 7. Neutral stability curves of (a) vortex-number, (b) angle and (c) wavenumber for a range of M and ϕ at $H = 0.1$ with isotropic $\lambda = 0.25, \eta = 0.25$.

The streamwise perturbation eigenfunction magnitudes where, we replace the notations of $\check{u}, \check{v}, \check{w}$ notations by $u, v, w, (|u|, |v|, |w|)$ for a variety of magnetic fields are plotted in Fig. 9, with axial flow values at $H = 0.1$ and $R = Rc + 25$ for the type I modes. Fig. 9 (a) shows that each eigenfunction of the $|u|$ profiles narrows as the magnetic field's range expands. Increasing the magnetic field's range in radial grooves results in a modest decrease in streamwise jets. The magnetic field's range exhibits a similar concentric grooves effect in isotropic roughness. All of these modifications must result from modifications to the corresponding mean flow profiles for MHD.

The azimuthal eigenfunction profiles are seen to move closer to the disk surface for fixed axial H with increase in the MHD and a greater movement near the disk surface as shown in Fig. 9 (b). This is due to a slight decrease in the maximum of the azimuthal eigenfunction profile $|v|$ caused by an increase in the range of magnetic field and the Lorentz creates the resistance in concentric grooves. As opposed to the effect of the increased magnetic field in concentric grooves, we find that the effect of the increased magnetic field in radial groove slightly grows the distance between the $|v|$ profiles and the disk surface. This effect is brought about by the type I modes slightly dominating the type II modes and we can eliminate the type II mode, as shown in fig.

Fig. 9 (c) Then, with a given axial flow $H = 0.1$, the axial $|w|$ profiles of the type I mode are shown for a different values of magnetic fields. Increased magnetic field in concentric grooves $\lambda = 0.25$ initially causes a decrease in the maximum of the $|w|$ profiles, as seen in Fig. 9.

(a). When the magnetic field M 's range is increased for radial grooves, we see that the maximum of $|w|$ significantly decreases. The maximum of the $|w|$ profiles is decreased in Fig. 9 (c) as the magnetic field increases in an isotropic roughness.

With roughness values at $H = 0.1$ and $R = Rc + 25$ for the type I modes, the streamwise perturbation eigenfunction magnitudes $(|u|, |v|, |w|)$ over a range of nanoparticles are plotted in Fig. 10. Fig. 10(a) shows how each eigenfunction of the $|u|$ profiles becomes narrower as the range of the ϕ increases. A slight decrease in streamwise jets occurs when the ϕ range for radial grooves is increased.

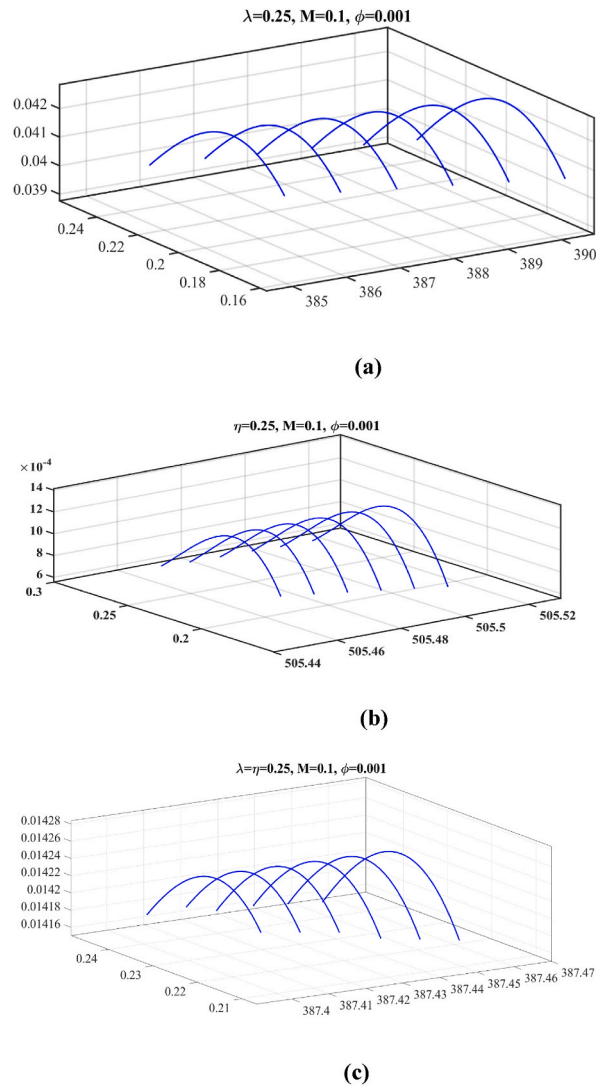


Fig. 8. Linear Convective Growth Rates of Stationary Disturbances at a fixed $H = 0.1$, $M = 0.1$ and $\phi = 0.001$ with various surface roughness (a) ($\eta = 0$, $\lambda = 0.25$), (b) ($\eta = 0.25$, $\lambda = 0$) and (c) ($\eta = 0.25 = \lambda$).

All of these variations must be the result of corresponding mean flow profile changes.

As illustrated in Fig. 10 (b), the azimuthal eigenfunction profiles are seen to move closer to the disk surface with fixed axial H and a greater movement of ϕ there. This is because an increase in the viscosity due to range of nanoparticles field in concentric grooves has led to a slight decrease in the maximum of the azimuthal eigenfunction profile $|v|$. As seen in Fig. 10 (c), the impact of various nanoparticles on radial grooves and isotropic grooves is similar with the effect on concentric grooves. The range of ϕ isotropic eigenfunction profile $|w|$ shows the same behavior as in Fig. 9 (c).

The energy balance estimate of the magnetic field's in isotropic roughness is shown in Fig. 11 (a). The calculation for energy balance has been demonstrated of type I mode instability of the magnetic field with anisotropic roughness $\lambda = 0.25$. In Fig. 11 (a) increasing MHD results in a significant stability of system as Total Energy (TE) is effective by the resistance of the Lorentz forces and lightly reduce the flows, which make the each flow in system more stable. In conclusion, the observed effect can be related mainly to the changes in the energy dissipation term (EDV) and the energy production term P_2 and there is reduction in the viscous magnetic field term G_5 . Fig. 11(b) displays the energy balance computation at various magnetic field strengths for inviscid type I modes, including $H = 0.1$. The graph shows changes in the energy generation factors, energy loss factors, and the overall energy (TE) of the system. Through investigation of these energy elements, we acquire understanding about the movement of energy and general characteristics of the type I modes without viscosity when exposed to varying magnetic field intensities. It is worth noting that the TE changes are less stable compared to the concentric grooves ($\lambda = 0.25$) case. In conclusion, when $\eta = 0.25$, there is a reduction in energy production, magnetic field term G_5 and a slight increase in energy dissipation. In Fig (c) the calculation for energy balance has been given for a various values of magnetic field in isotropic roughness ($\lambda = \eta = 0.25$) and $H = 0.1$ the axial flow. The inviscid type I

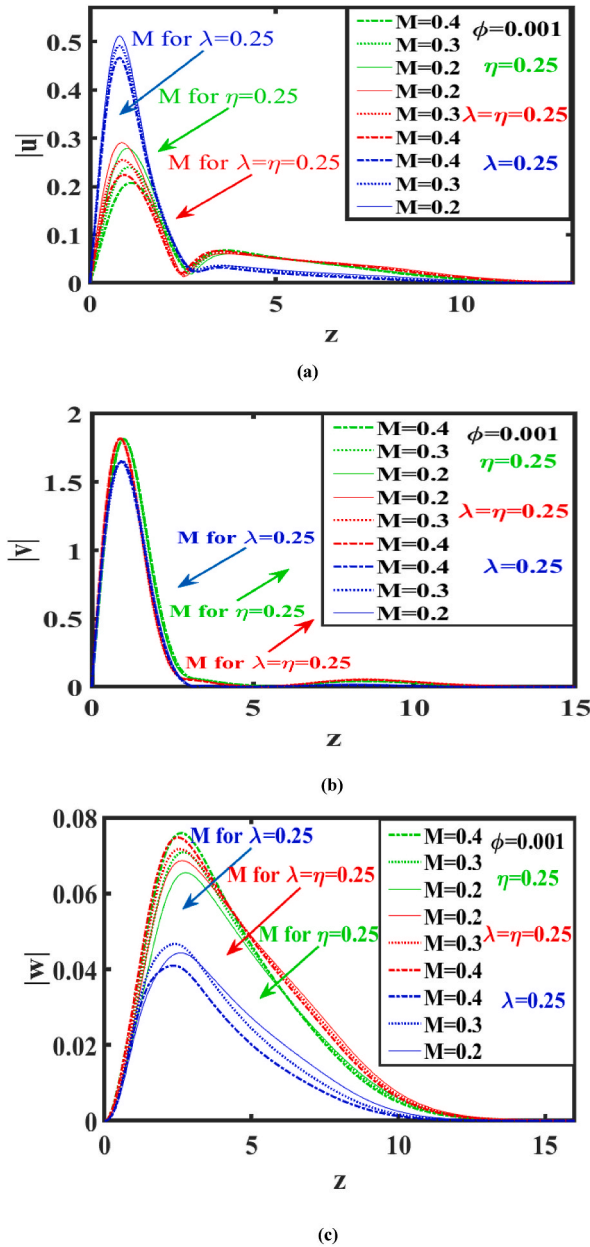


Fig. 9. Eigenfunctions for a range MHD with fixed axial flow $H = 0.1$ for various roughness.

instability, also known as cross-flow instability, experiences a considerable stabilizing effect in this situation. This is mainly due to changes in the energy dissipation of the system (EDV). The instability's growth and amplification are reduced due to alterations in energy dissipation, resulting in a more stable flow behavior. In conclusion, a higher value of MHD results in increased stability of the system. This is particularly evident when the MHD value is large.

The energy balance estimate of the nanoparticles in isotropic roughness is shown in Fig. 12 (a). It is obvious that a stabilization effect was achieved in the Type I mode as a result of a slight decrease in the flow's total energy as the φ parameter is raised due to the viscous effect nanoparticles. The reduction in energy production term P_2 , viscous term of nanofluids G_5 and energy dissipation term EDV is the main basis of this effect. The modifications to the other terms seems to be negligible. In Fig. 12 (b), it is evident that a stabilizing effect was obtained in the Type I mode lightly less than Fig. 12 (a). The increase in the energy production term P_2 and the energy dissipation term D is the main source of this impact when φ parameter is increased. Fig. 12 (c) shows the similar result as Fig. 12 (b),

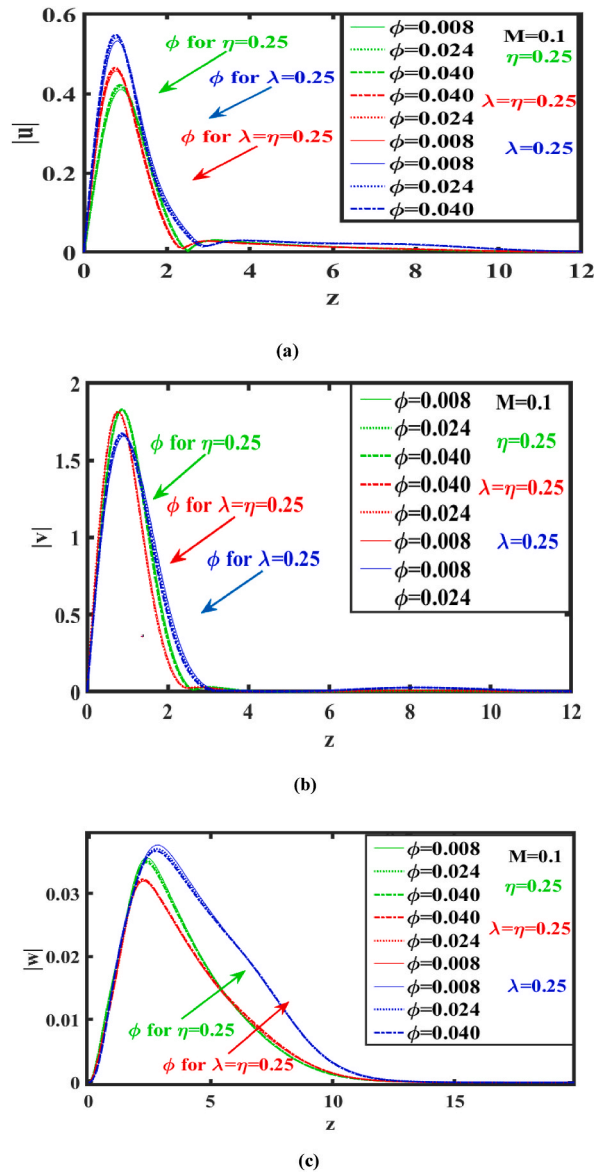


Fig. 10. Eigenfunction for a range ϕ with fixed axial flow $H = 0.1$ for various roughness.

7. Summary and conclusion

We have investigated the MHD of Cu-water nanofluid over a rotating disk with the enforced axial flow for anisotropic and isotropic roughness. The main aim of this work is to focus on convective instability with MHD of nanofluid over a rough rotating disk which involves the study of stationary modes of disturbances for MHD. The no-slip boundary conditions are changed into partial slip boundary conditions by using MW [9] approach with simulation when isotropic in the radial direction and anisotropic in the azimuthal direction. Additionally, we developed the steady boundary-layer flow across a disk-mounted rotating reference frame.

When we increased the range of the MHD nanofluid for different ranges of enforced axial flow with anisotropic and isotropic roughness. MATLAB is used for the results as shooting method for the mean-flow and chebyshev polynomial discretization for neutral stability curves results. We observed the following results from their influence on boundary layer flow:

- In all the cases we observed the boundary-layer thinning for each flow.
- We obtained the inviscid type I mode stabilized the most effectively and increased the critical Reynolds number.
- The study also showed how the combination of MHD of nanofluid can cause stationary instability modes through a receptivity mechanism. The modes are caused by zero frequency disturbances and magnetic fields and the volume fraction of nanoparticles affects the stability of a system at a specific wavelength, causing instability.

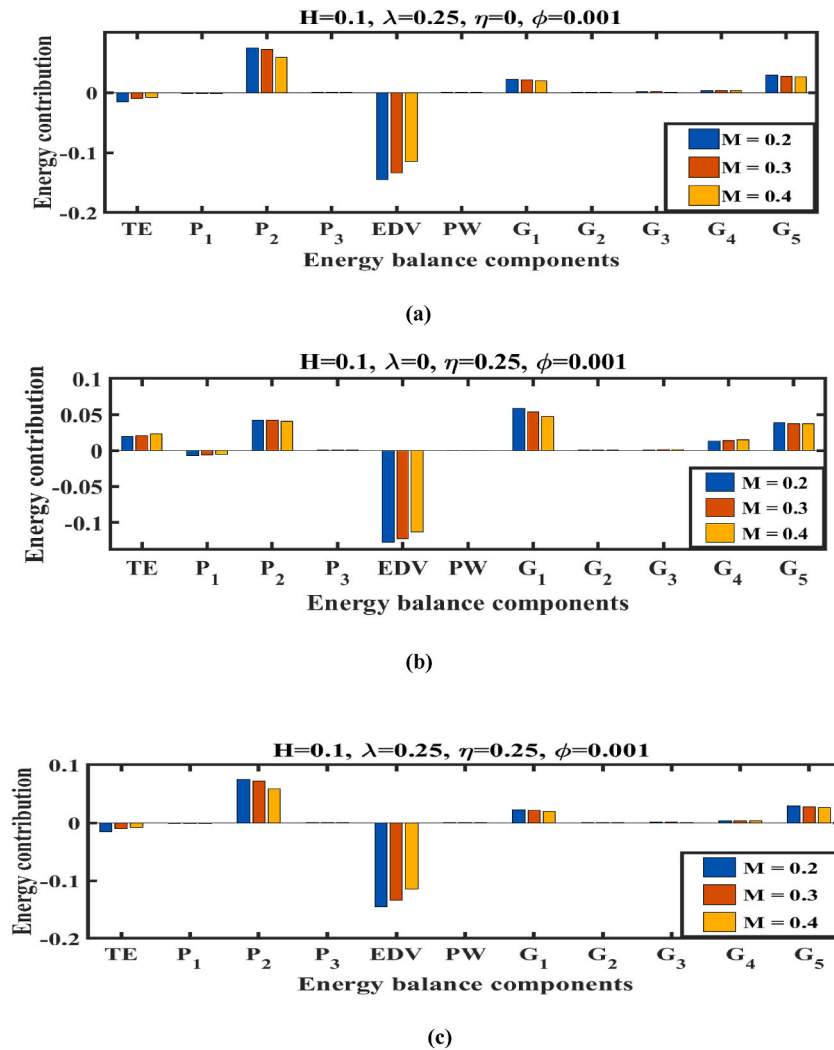
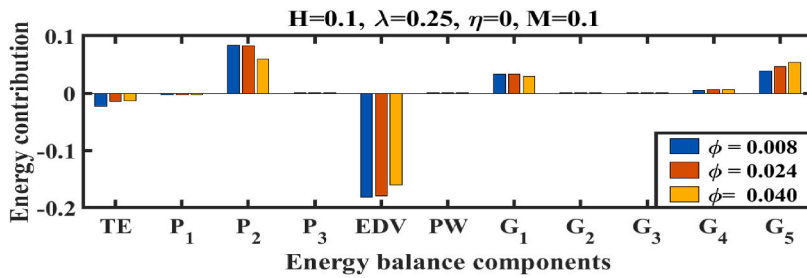


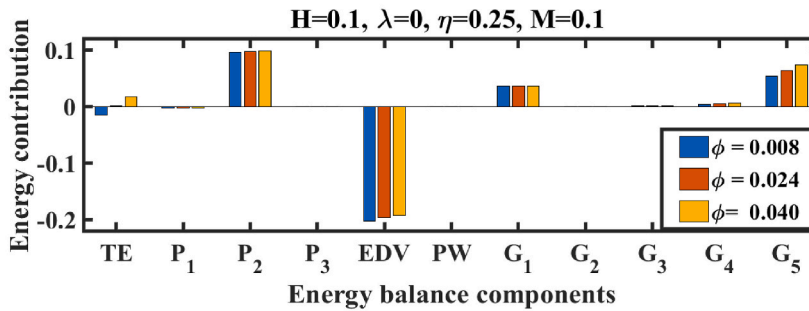
Fig. 11. Energy Contribution of Individual Components at Fixed $\phi = 0.001$ and Axial Flow $H = 0.1$ with varying magnetic field on Type I Instability Mode on variable roughness (a) for $\lambda = 0.25, \eta = 0$ (b) for $\eta = 0.25, \lambda = 0$ (c) for $\lambda = \eta = 0.25$.

- It is discovered that instability is more strong in concentric grooves for the range of a magnetic field than isotropic roughness and reduces the amplification rates of stationary modes.
- According to our physical predictions, as the axial flow rate is increased in the presence of magnetic field and volume fractions of nanoparticles for different surfaces, fluid is forced toward the disk’s surface. This causes the development of a destabilizing impact of viscous effects within the wall location.
- In fixed axial flows over a rough disk, increased magnetic field ranges reduce the unstable regime’s maximum growth rates.
- Reduction of the first type mode’s energy generation and dissipation in the presence of MHD of nanofluid with anisotropic roughness’s and isotropic roughness reduces the total energy, which is further evidence that supports our results. We can find the stability for the large number of magnetic fields but due to the roughness and volume fraction of nanoparticles involved in the boundary condition, we are restricted.

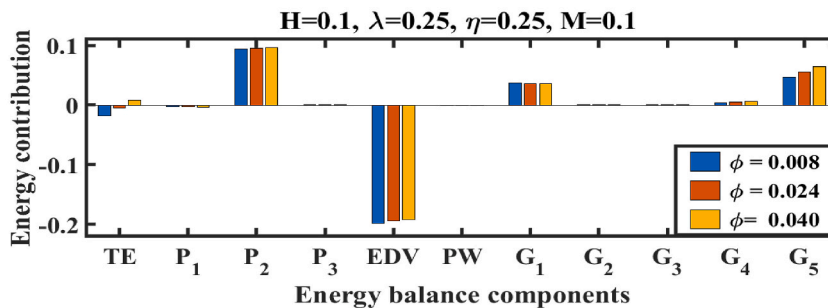
The study’s conclusions state that the findings apply to a wide range of engineering applications and serve as a useful passive flow-control system for engineering flows over rotating surfaces that involve magnetic fields, rough disks, and other cross-flow dominant flows. The turbulence of a fluid’s velocity can be controlled by magnetic strength. Due to their importance in practical applications, magnetic effects on lubricating fluids have attracted great interest. According to our research, it is preferable to increase the strength of the axial flow over a rough disk because it may help to maintain laminar flow, in the support disk, over a greater area for a variety of magnetic fields. The fluid velocity across the disk surface tends to decrease because of the “Lorentz force,” a retarding impact caused by the induction of magnetic upshot. This investigation demonstrates that the choice of surface roughness with more care along the range of enforced axial flow, magnetic field, and volume fraction of nanoparticles leads to a stabilization in the flows that may be seen in



(a)



(b)



(c)

Fig. 12. Energy Contribution of Individual Components at Fixed $M = 0.1$ and Axial Flow $H = 0.1$ with varying ϕ on Type I Instability Mode on variable roughness (a) for $\lambda = 0.25, \eta = 0$ (b) for $\eta = 0.25, \lambda = 0$ (c) for $\lambda = \eta = 0.25$.

numerous applications of engineering.

Data availability statements

The authors states that all the files are provided in the paper no hidden file is required however if journal required any further data from us we will provide and the corresponding author is responsible to provide to the journal.

CRedit authorship contribution statement

Tousif Iqra: Formal analysis, Data curation, Conceptualization. **Sohail Nadeem:** Writing – review & editing, Supervision, Project administration, Investigation, Conceptualization. **Hassan Ali Ghazwani:** Writing – original draft, Visualization, Software, Resources, Methodology. **Faisal Z. Duraihem:** Writing – review & editing, Writing – original draft, Visualization, Validation, Software. **Jehad Alzabut:** Writing – review & editing, Validation, Formal analysis.

Declaration of competing interest

The authors declared that they do not have any conflict of interest.

Acknowledgement

(Researchers Supporting Project number (RSPD2024R535), King Saud University, Riyadh, Saudi Arabia).
S. Nadeem and Jehad Alzabut are Thankful to PSU for the Support of this Paper.

References

- [1] K.S. Choi, The rough with the smooth, *Nature* 440 (7085) (2006) 754, <https://doi.org/10.1038/440754a>, 754.
- [2] L. Sirovich, S. Karlsson, Turbulent drag reduction by passive mechanisms, *Nature* 388 (6644) (1997) 753–755, <https://doi.org/10.1038/41966>.
- [3] Th V. Kármán, Über laminare und turbulente Reibung, *Z. Angew. Math. Mech.* 1 (1921) 233–252, <https://doi.org/10.1002/zamm.19210010401>.
- [4] N. Gregory, J.T. Stuart, W.S. Walker, On the stability of three-dimensional boundary layers with application to the flow due to a rotating disk, *Philos. Trans. Royal Soc.* 248 (943) (1955) 155–199, <https://www.jstor.org/stable/91581>.
- [5] M.R. Malik, The neutral curve for stationary disturbances in rotating-disk flow, *J. Fluid Mech.* 164 (1986) 275–287, <https://doi.org/10.1017/S0022112086002550>.
- [6] P. Hall, An asymptotic investigation of the stationary modes of instability of the boundary layer on a rotating disc, *Proc. Math. Phys. Eng. Sci.* 406 (1830) (1986) 93–106, <https://doi.org/10.1098/rspa.1986.0066>.
- [7] T. Watanabe, H.M. Warui, N. Fujisawa, Effect of distributed roughness on laminar-turbulent transition in the boundary layer over a rotating cone, *Exp. Fluid* 14 (5) (1993) 390–392, <https://doi.org/10.1007/BF00189498>.
- [8] M.S. Yoon, J.M. Hyun, J.S. Park, Flow and heat transfer over a rotating disk with surface roughness, *Int. J. Heat Fluid Flow* 28 (2) (2007) 262–267, <https://doi.org/10.1016/j.ijheatfluidflow.2006.04.008>.
- [9] M. Miklavčić, C.Y. Wang, The flow due to a rough rotating disk, *Z. Angew. Math. Phys.* 55 (2004) 235–246, <https://doi.org/10.1007/s00033-003-2096-6>.
- [10] A.J. Cooper, J.H. Harris, S.J. Garrett, M. Özkan, P.J. Thomas, The effect of anisotropic and isotropic roughness on the convective stability of the rotating disk boundary layer, *Phys. Fluids* 27 (1) (2015) 014107, <https://doi.org/10.1063/1.4906091>.
- [11] S.J. Garrett, A.J. Cooper, J.H. Harris, M. Özkan, A. Segalini, P.J. Thomas, On the stability of von Kármán rotating-disk boundary layers with radial anisotropic surface roughness, *Phys. Fluids* 28 (1) (2016) 014104, <https://doi.org/10.1063/1.4939793>.
- [12] H.P. Pao, Magnetohydrodynamic flows over a rotating disk, *AIAA J.* 6 (7) (1968) 1285–1291, <https://doi.org/10.2514/3.4735>.
- [13] H.A. Jasmine, J.S.B. Gajjar, Convective and absolute instability in the incompressible boundary layer on a rotating disk in the presence of a uniform magnetic field, *J. Eng. Math.* 52 (4) (2005) 337–353, <https://doi.org/10.1007/s10665-005-2732-6>.
- [14] M. Turkyilmazoglu, Resonance instabilities in the boundary-layer flow over a rotating-disk under the influence of a uniform magnetic field, *J. Eng. Math.* 59 (2007) 337–350, <https://doi.org/10.1007/s10665-007-9137-7>.
- [15] X.Q. Wang, A.S. Mujumdar, A review on nanofluids-part II: experiments and applications, *Braz. J. Chem. Eng.* 25 (4) (2008) 631–648, <https://doi.org/10.1590/s0104-66322008000400002>.
- [16] K.V. Wong, O.D. Leon, Applications of nanofluids: current and future, *Adv. Mech. Eng.* 2 (2010) 519659, <https://doi.org/10.1155/2010/519659>.
- [17] N. Bachok, A. Ishak, R. Nazar, I. Pop, Flow and heat transfer at a general three-dimensional stagnation point in a nanofluid, *Physica B: Condens.* 405 (24) (2010) 4914–4918, <https://doi.org/10.1016/j.physb.2010.09.031>.
- [18] N. Bachok, A. Ishak, I. Pop, Flow and heat transfer characteristics on a moving plate in a nanofluid, *Int. J. Heat Mass Tran.* 55 (4) (2012) 642–648, <https://doi.org/10.1016/j.ijheatmasstransfer.2011.10.047>.
- [19] T. Grosan, I. Pop, Axisymmetric mixed convection boundary layer flow past a vertical cylinder in a nanofluid, *Int. J. Heat Mass Tran.* 54 (15–16) (2011) 3139–3145, <https://doi.org/10.1016/j.ijheatmasstransfer.2011.04.018>.
- [20] N.A. Yacob, A. Ishak, I. Pop, Falkner–Skan problem for a static or moving wedge in nanofluids, *Int. J. Therm. Sci.* 50 (2) (2011) 133–139, <https://doi.org/10.1016/j.ijthermalsci.2010.10.008>.
- [21] M.A.S. Al-Malki, S.J. Garrett, S. Camarri, Z. Hussain, The effects of roughness levels on the instability of the boundary-layer flow over a rotating disk with an enforced axial flow, *Phys. Fluids* 33 (10) (2021) 104109, <https://doi.org/10.1063/5.0064132>.
- [22] B. Alveroglu, A. Segalini, S.J. Garrett, The effect of surface roughness on the convective instability of the BEK family of boundary-layer flows, *Eur. J. Mech. B Fluid* 56 (2016) 178–187.
- [23] F. Wang, M. Awais, R. Parveen, M.K. Alam, S. Rehman, N.A. Shah, Melting rheology of three-dimensional Maxwell Nanofluid (Graphene-Engine-Oil) flow with slip condition past a stretching surface through Darcy-Forchheimer medium, *Results Phys.* (2023) 106647, <https://doi.org/10.1016/j.rinp.2023.106647>.
- [24] F. Wang, N. Tarakaramu, M.V. Govindaraju, N. Sivakumar, K.B. Lakshmi, P. S. Narayana, R. Sivajothi, Activation energy on three-dimensional Casson nanofluid motion via stretching sheet: implementation of Buongiorno's model, *J. Indian Chem. Soc.* 100 (2) (2023) 100886, <https://doi.org/10.1016/j.jics.2023.100886>.
- [25] F. Wang, M.I. Asjad, M. Zahid, A. Iqbal, H. Ahmad, M.D. Alsulami, Unsteady thermal transport flow of Casson nanofluids with generalized Mittag-Leffler kernel of Prabhakar's type, *J. Mater. Res. Technol.* 14 (2021) 1292–1300, <https://doi.org/10.1016/j.jmrt.2021.07.029>.